

SHORT-TERM RADIO VARIABILITY AND PARSEC-SCALE STRUCTURE IN A GAMMA-RAY NARROW-LINE SEYFERT 1 GALAXY 1H 0323+342

KIYOAKI WAJIMA¹, KENTA FUJISAWA^{2,3}, MASAAKI HAYASHIDA⁴, NAOKI ISOBE⁵,
 TAKAFUMI ISHIDA³, AND YOSHINORI YONEKURA⁶

¹ Shanghai Astronomical Observatory, Chinese Academy of Sciences, 80 Nandan Road,
 Xuhui District, Shanghai 200030, China; kwajima@shao.ac.cn

² The Research Institute for Time Studies, Yamaguchi University, 1677-1 Yoshida, Yamaguchi, Yamaguchi 753-8511, Japan

³ Graduate School of Science and Engineering, Yamaguchi University, 1677-1 Yoshida, Yamaguchi, Yamaguchi 753-8512, Japan

⁴ Institute for Cosmic Ray Research, The University of Tokyo, 5-1-5 Kashiwanoha, Kashiwa, Chiba 277-8582, Japan

⁵ The Institute of Space and Astronautical Science, Japan Aerospace Exploration Agency,
 3-1-1 Yoshinodai, Chuo-ku, Sagami-hara, Kanagawa 252-5210, Japan

⁶ Center for Astronomy, Ibaraki University, 2-1-1 Bunkyo, Mito, Ibaraki 310-8512, Japan

Received 2013 June 14; accepted 2013 December 10; published 2014 January 10

ABSTRACT

We made simultaneous single-dish and very long baseline interferometer (VLBI) observations of a narrow-line Seyfert 1 galaxy 1H 323+342, showing gamma-ray activity revealed by *Fermi*/Large Area Telescope observations. We found significant variation of the total flux density at 8 GHz on the timescale of one month by the single-dish monitoring. The total flux density varied by 5.5% in 32 days, which is comparable to the gamma-ray variability timescale, corresponding to the variability brightness temperature of 7.0×10^{11} K. The source consists of central and southeastern components on the parsec (pc) scale. Only the flux of the central component decreased in the same way as the total flux density, indicating that the short-term radio variability, and probably the gamma-ray-emitting region, is associated with this component. From the VLBI observations, we obtained brightness temperatures of greater than $(5.2 \pm 0.3) \times 10^{10}$ K and derived an equipartition Doppler factor of greater than 1.7, a variability Doppler factor of 2.2, and an 8 GHz radio power of $10^{24.6}$ W Hz⁻¹. Combining them, we conclude that acceleration of radio jets and creation of high-energy particles are ongoing in the central engine and that the apparent very radio-loud feature of the source is due to the Doppler boosting effect, resulting in the intrinsic radio loudness being an order of magnitude smaller than the observed values. We also conclude that the pc-scale jet represents recurrent activity from the spectral fitting and the estimated kinematic age of pc- and kpc-scale extended components with different position angles.

Key words: galaxies: active – galaxies: individual (1H 0323+342) – galaxies: Seyfert – radio continuum: galaxies – techniques: interferometric

Online-only material: color figures

1. INTRODUCTION

Gamma-ray emission from active galactic nuclei (AGNs) is one of the important properties in terms of activities and energetics of the central engine and emergence of relativistic jets. In the Energetic Gamma-Ray Experiment Telescope era, nearly 100 gamma-ray emitting AGNs were known (Hartman et al. 1999; Sowards-Emmerd et al. 2003, 2004). They are predominantly radio-loud AGNs and are categorized as blazars, suggesting a close connection between gamma-ray and radio emission. On the other hand, observations with the *Fermi* Gamma-ray Space Telescope (hereafter *Fermi*) have resulted in the identification of more than a thousand AGNs, some of which are categorized as nonblazar active galaxies or radio galaxies (Nolan et al. 2012). Moreover, *Fermi* has also revealed the existence of new classes of gamma-ray-emitting AGNs, one of which is a narrow-line Seyfert 1 galaxy (NLS1). NLS1 is a subclass of AGNs and is identified by its optical properties: narrow permitted lines, $\text{FWHM}(\text{H}\beta) < 2000 \text{ km s}^{-1}$, emitted from the broad line region, $[\text{O III}]/\text{H}\beta < 3$, and a bump due to Fe II (Osterbrock & Pogge 1985; Pogge 2000).

The first detection of gamma-ray emission in a radio-loud NLS1 by *Fermi* was made for PMN J0948+0022 (Abdo et al. 2009a). Intensive observations by the Large Area Telescope (LAT) on board *Fermi* have revealed new detections of gamma

rays of other three radio-loud NLS1s (Abdo et al. 2009b). To date, seven NLS1s are listed as gamma-ray sources detected by *Fermi*/LAT (Foschini 2011), and the number of gamma-ray NLS1s is increasing.⁷ These are surprising discoveries because most NLS1s are hosted in a spiral galaxy, which usually does not have relativistic jets, whereas blazars are hosted in an elliptical galaxy. Although milliarcsecond (mas)-scale images have been obtained for several gamma-ray NLS1s with very long baseline interferometer (VLBI) observations (Doi et al. 2006b, 2007; Giroletti et al. 2011; Linford et al. 2012; Orienti et al. 2012; D’Ammando et al. 2012, 2013) and some of them have revealed the presence of a closely aligned relativistic jet, there are still large uncertainties for the derived parameters in gamma-ray NLS1s, and it is therefore important to investigate the parsec (pc)-scale properties.

NLS1s are also considered to have high mass accretion rates, close to the Eddington limit, and lower black hole masses ($M_{\text{BH}} \sim 10^{5-7} M_{\odot}$) compared to other classes of AGNs (Boroson 2002). Considering the relation among radio loudness, the black hole mass, and the accretion rate (Greene et al. 2006; Zhou et al. 2007 and references therein), those properties imply that NLS1s are generally radio-quiet objects and have weak or no jet activity (Maccarone et al. 2003). In fact, previous studies show that the fraction of radio-loud NLS1s is low (about 7%)

⁷ See <http://www.brera.inaf.it/utenti/foschini/gNLS1/catalog.html>.

Table 1
Summary of JVN Observations and Description of JVN Images

Epoch	Date	Telescopes	θ_{Bmaj}	θ_{Bmin}	P.A.	S_{peak}	σ	S_{CLEAN}
(1)	(UT)	(3)	(mas)	(mas)	(deg)	(mJy beam ⁻¹)	(mJy beam ⁻¹)	(mJy)
(1)	(2)	(3)	(4)	(5)	(6)	(7)	(8)	(9)
1	2010 Nov 1 11:00–21:00	VERA, HIT	3.52	1.81	124.0	397	3.1	467
2	2010 Nov 15 10:00–20:00	VERA, HIT, KAS	3.73	1.85	126.0	298	2.8	359
3	2010 Nov 30 09:00–19:00	VERA, HIT, KAS	3.77	1.80	124.5	272	2.2	335

Notes. Columns are as follows: (1) JVN observation epoch; (2) observation date; (3) telescopes (VERA: VERA (4×20 m), HIT: Hitachi 32 m, KAS: Kashima 34 m); (4)–(6) parameters of the restoring beam: FWHM of major and minor axes and the position angle of the major axis; (7) peak intensity; (8) rms noise level; (9) total CLEANed flux.

compared to other AGN classes (Komossa et al. 2006) and that NLS1s have lower jet activities compared to other types of radio-loud AGNs (Greene et al. 2006; Zhou et al. 2006). NLS1s are thus considered to be at the high/soft state containing a slim disk, whereas blazars and flat-spectrum radio quasars are at the low/hard state, in the analogy of Galactic X-ray binaries (Mineshige et al. 2000; Maccarone et al. 2003). It is interesting to study the relation between the state transition and the jet activity in AGNs since we can import knowledge of the state transition for Galactic X-ray binaries to AGNs. Again, multiepoch and high-resolution radio observations are essential to investigate them.

In this paper, we report the results of simultaneous single-dish and VLBI observations of 1H 0323+342 at 8 GHz, including the archival data obtained by the Very Long Baseline Array (VLBA). 1H 0323+342 is one of seven gamma-ray-emitted NLS1s detected by *Fermi*/LAT (Abdo et al. 2009b). An optical observation by the *Hubble Space Telescope* shows that the source is hosted in a spiral galaxy containing a single spiral arm (Zhou et al. 2007), whereas another results claim that the host galaxy of the source has a ring structure triggered by an interacting/merging process (Antón et al. 2008). M_{BH} is estimated to be a few times $10^7 M_{\odot}$ with a few different methods using the width and luminosity of the H β line and the continuum luminosity at 5100 Å (Zhou et al. 2007). This is in good agreement with $M_{\text{BH}} = 10^{7.0} M_{\odot}$ from the parameter used to model the spectral energy distribution (Abdo et al. 2009b). Abdo et al. (2009b) estimate the accretion disk luminosity to be $1.4 \times 10^{45} \text{ erg s}^{-1}$, or $0.9 L_{\text{Edd}}$, where L_{Edd} is the Eddington luminosity. Although these characteristics are typically seen among NLS1s, the source has extremely high radio loudness $R_{1.4} = f_{1.4 \text{ GHz}}/f_{440 \text{ nm}} = 318$ (Foschini 2011), or $R_5 = f_{5 \text{ GHz}}/f_{440 \text{ nm}} = 246$ (Doi et al. 2012), and is listed in one of 29 very radio-loud ($R > 100$) NLS1s (Foschini 2011), implying activities due to relativistic jets in the inner region. A redshift z of 0.0629 ± 0.0001 is measured by Zhou et al. (2007), and we adopt this value, although some previous studies adopt $z = 0.061$ as reported by Marchã et al. (1996). 1H 0323+342 is the nearest object among gamma-ray NLS1s, allowing us to investigate the inner region of the source with higher angular resolution.

The contents of this paper are as follows. Our observations and data reduction procedures are described in Section 2. We present the results of single-dish and VLBI observations in Section 3. In Section 4, we describe the results of the archival VLBA observations. In Section 5, we discuss the observed variability feature, the relation to general properties of NLS1s, and possible connections between gamma-ray emission and the pc-scale structure. The achievements of our study are summarized in Section 6. Throughout this paper, we define the spectral index α as $S_{\nu} \propto \nu^{+\alpha}$, where S_{ν} is the flux density at the frequency

ν , and we adopt a Λ cold dark matter (Λ CDM) cosmology with $H_0 = 71 \text{ km s}^{-1} \text{ Mpc}^{-1}$, $\Omega_{\Lambda} = 0.73$, and $\Omega_{\text{M}} = 0.27$ from the results of the *Wilkinson Microwave Anisotropy Probe* (Komatsu et al. 2009), corresponding to an angular-to-linear scale conversion of 1.20 pc mas^{-1} for 1H 0323+342.

2. OBSERVATIONS AND DATA REDUCTION

The total flux density of 1H 0323+342 was monitored by the Yamaguchi 32 m radio telescope (hereafter Y32; Fujisawa et al. 2002) at 25 epochs from 2010 November 9 (2010.858) to 2011 February 5 (2011.099). The Y32 observations were made typically every two or three days. The monitoring was done at 8.38 GHz with a total bandwidth of 400 MHz in the total power mode. We employed the “Z-scan” method to remove both the gain and atmospheric fluctuations and the pointing offsets. A detailed procedure of the observation and data reduction of the method is described by Kadota et al. (2012). The flux density of 1H 0323+342 was measured by comparing the total received power with that of a strong, nearby radio source, 3C 123 (9.310 Jy; Ott et al. 1994).

Observations with the Japanese VLBI Network (JVN; Doi et al. 2006a) were made simultaneously with Y32 monitoring at three epochs in 2010 November. The observation dates of each epoch are shown in Table 1. Six radio telescopes, four telescopes from the VLBI Exploration of Radio Astrometry (VERA; Kobayashi et al. 2003) with an antenna diameter of 20 m each, the Hitachi 32 m telescope (Yonekura et al. 2013), and the Kashima 34 m telescope, were used for the observations, although Kashima did not participate in epoch 1. Observations were made in right-circular polarization at 8.424 GHz with a total bandwidth of 32 MHz. Observed sources were 1H 0323+342 as a target, J0310+3814 as a gain calibrator (separation angle of $4^{\circ}.94$ from 1H 0323+342), DA 193 as a flux calibrator, and 3C 84 as a bandpass calibrator. The total on-source duration for 1H 0323+342 is 443 minutes in all epochs. The data were correlated using the Mitaka FX correlator (Shibata et al. 1998) with an output preaveraging time of 2 s.

The JVN data were reduced using the Astronomical Image Processing System (AIPS) software (Greisen 2003) for amplitude and phase calibration and the Caltech software Difmap (Shepherd 1997) for imaging and self-calibration. We did not employ a standard a priori amplitude calibration using the system noise temperature because it was not measured during the observations at several stations. Flux densities of each source were therefore determined as follows. We determined the flux density of DA 193 by single-dish observations with Y32 to be $4.787 \pm 0.027 \text{ Jy}$ on 2010 November 15 and $4.907 \pm 0.040 \text{ Jy}$ on 2010 November 29. We assumed the correlated flux density of DA 193 with JVN to be same as that with single-dish

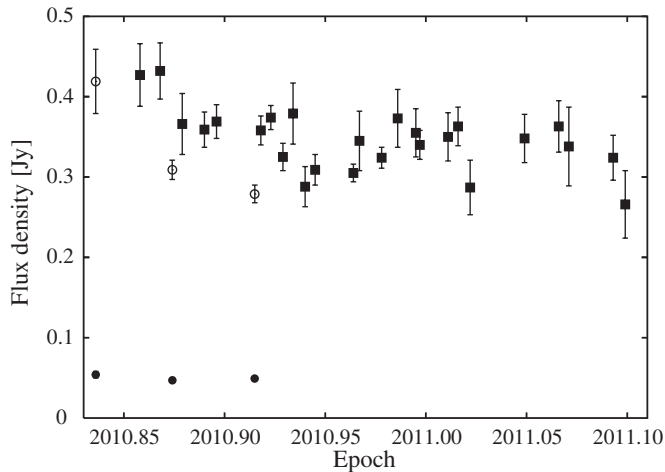


Figure 1. The 8.4 GHz light curve of 1H 0323+342. The filled squares show the total flux obtained with the Yamaguchi 32 m radio telescope. The numerical data of the measurements are shown in Table 2. The open and filled circles indicate the flux of components C and D1, respectively, obtained with the JVN observations (see also Section 3.2 and Table 1).

measurements since DA 193 can be considered as a point source within the JVN baseline lengths. Flux densities were determined comparing cross-correlation amplitudes for each source with those for DA 193. To correct the variation of the antenna gain due to the change of the antenna elevation, we applied self-calibration to the gain calibrator J0310+3814. It can be considered a point source and was observed once an hour with an on-source duration of 5 minutes per scan. A fitted curve to the solutions for the gain calibrator was applied to other sources.

Through the procedure described above, we determined flux densities of J0310+3814 at epochs 2 and 3 to be comparable to previous results by VLBI observations at the same frequency. On the other hand, the flux density of J0310+3814 at epoch 1, obtained by the AIPS task GETJY, was determined to be twice (1.913 Jy) than that at epochs 2 (0.985 Jy) and 3 (0.989 Jy). We finally determined a flux density of J0310+3814 at epoch 1 to be same as that obtained at epoch 2 for the following reasons. At epochs 2 and 3, both the Kashima 34 m and Hitachi 32 m telescopes participate in the observations. Those antennas have system-equivalent flux densities approximately seven times better than those of four VERA antennas at 8 GHz. We therefore consider the results at epochs 2 and 3 to be more likely than that at epoch 1. In addition, we obtain similar flux densities at epochs 2 and 3, as mentioned above. We therefore consider that J0310+3814 does not show variability during the JVN campaign.

We exported the calibrated visibility data to Difmap for imaging. The amplitude calibration error obtained with the self-calibration procedure was 10%, 4%, and 4% for each epoch. To ensure a better angular resolution, we adopt uniform weighting of the data with gridding weights scaled by amplitude errors raised to the power of -1 . The maximum and minimum projected baseline lengths of the JVN observation were 2290 km, or 64 M λ (VERA Mizusawa–VERA Ishigakijima baseline), and 77 km, or 2.2 M λ (Hitachi–Kashima baseline), respectively.

3. RESULTS

3.1. Single-dish Monitoring with the Yamaguchi 32 m Radio Telescope

Figure 1 shows the total flux density measurements of 1H 0323+342 by Y32. Numerical data of the measurements are

Table 2
Results of the Total Flux Measurement at 8.38 GHz with the Yamaguchi 32 m Radio Telescope

Date	Epoch	$S_{8\text{GHz}}$ (mJy)	N^a
2010 Nov 9	2010.858	427 ± 28	31
2010 Nov 13	2010.868	432 ± 24	35
2010 Nov 17	2010.879	366 ± 27	32
2010 Nov 21	2010.890	359 ± 16	39
2010 Nov 23	2010.896	369 ± 15	38
2010 Dec 1	2010.918	358 ± 18	39
2010 Dec 3	2010.923	374 ± 11	39
2010 Dec 5	2010.929	325 ± 12	39
2010 Dec 7	2010.934	379 ± 27	38
2010 Dec 9	2010.940	288 ± 18	38
2010 Dec 11	2010.945	309 ± 13	40
2010 Dec 18	2010.964	305 ± 8	39
2010 Dec 19	2010.967	345 ± 26	26
2010 Dec 23	2010.978	324 ± 9	36
2010 Dec 26	2010.986	373 ± 25	24
2010 Dec 29	2010.995	355 ± 21	31
2010 Dec 30	2010.997	340 ± 13	39
2011 Jan 4	2011.011	350 ± 21	26
2011 Jan 6	2011.016	363 ± 17	36
2011 Jan 8	2011.022	287 ± 24	25
2011 Jan 18	2011.049	348 ± 21	17
2011 Jan 24	2011.066	363 ± 23	18
2011 Jan 26	2011.071	338 ± 35	12
2011 Feb 3	2011.093	324 ± 20	15
2011 Feb 5	2011.099	266 ± 30	12

Note. ^a Number of independent measurements.

shown in Table 2. Error bars at each point in Figure 1 indicate a 1σ standard deviation divided by the square root of the number of independent measurements. The source was also monitored between 2010.6 and 2011.2 at nine frequencies from 2.64 to 142 GHz by the F-GAMMA Program (Fuhrmann et al. 2011; Angelakis et al. 2012). Our results are in good agreement with theirs at 8.35 GHz, within the margin of error. F-GAMMA results show that the flux density varies almost simultaneously at observing frequencies from 2.64 to 32.0 GHz (Fuhrmann et al. 2011); therefore, we believe that the flux variation observed with Y32 is intrinsic. The total flux varies significantly during the period of Y32 monitoring compared with the constant flux. The maximum and minimum flux densities during Y32 monitoring can be seen as 432 ± 24 mJy on 2010 November 13 and 266 ± 30 mJy on 2011 February 5, respectively, corresponding to a flux decrease of 38% in 84 days, whereas the total flux does not decrease monotonically. We apply a third-order polynomial to all measurements of Y32 to estimate the local minimum and maximum of the flux densities (reduced $\chi^2 = 3.61$ with 23 degrees of freedom (dof) and 2.33 with 21 dof for linear and cubic functions, respectively, which is significant at $>99.9\%$ confidence level). The local minimum of 325 mJy at epoch 2010.956 and the local maximum of 344 mJy at epoch 2011.043 are derived from the best-fit curve, corresponding to a flux variation of 5.5% in 32 days. Whereas Fuhrmann et al. (2011) pointed out that the source indicates variability on timescales of months to years, our results clearly show the existence of the short-term radio variability on a timescale of 1 month. Moreover, this is comparable to the (*e*-folding) gamma-ray variability timescale of 17.7 ± 14.4 days from the 2 yr monitoring results from 2008 September to 2010 September by *Fermi*/LAT (Calderone et al. 2011), suggesting that the source

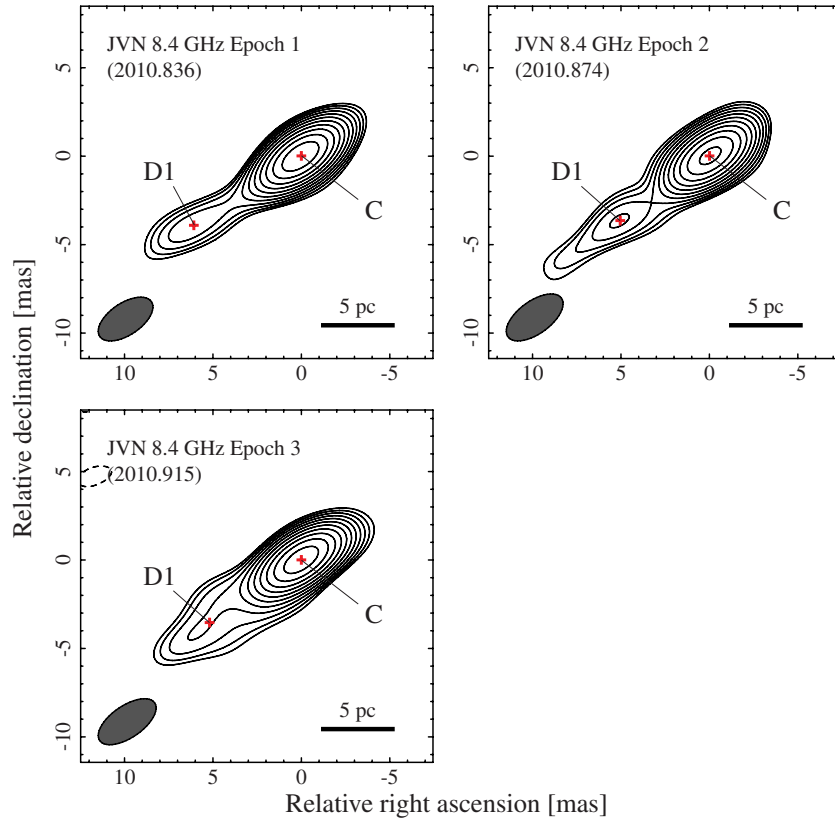


Figure 2. VLBI images of 1H 0323+342 at epochs 1 (top left), 2 (top right), and 3 (bottom) obtained by the JVN observations at 8.4 GHz. The lowest contour is three times the off-source rms noise (σ). The contour levels are $-3\sigma, 3\sigma \times (\sqrt{2})^n$ ($n = 0, 1, 2, \dots, 10$). The dashed and solid curves show negative and positive contours, respectively. The restoring beam is indicated in the lower left corner of each image. The labels C and D1 show the Gaussian model fitting components, and the position of each component is indicated by a cross. The image descriptions are given in Table 1.

(A color version of this figure is available in the online journal.)

Table 3
Model Fitting Results for JVN Observations

Epoch	Comp.	S (mJy)	r (mas)	ϕ (deg)	θ_{maj} (mas)	θ_{min} (mas)	P.A. (deg)	$T_{\text{B,rest}}^{(\text{image})}$ (10^{10} K)
(1)	(2)	(3)	(4)	(5)	(6)	(7)	(8)	(9)
1	C	419 ± 40	$<1.12 \pm 0.11$	$<0.12 \pm 0.01$	131.1 ± 0.4	$>8.3 \pm 1.3$
	D1	54 ± 4	7.22 ± 0.17	122.8 ± 2.1	3.76 ± 0.38	0.11 ± 0.01	116.5 ± 2.7	...
2	C	309 ± 12	$<0.59 \pm 0.02$	$<0.24 \pm 0.01$	84.6 ± 0.5	$>5.8 \pm 0.4$
	D1	47 ± 1	6.25 ± 0.13	125.8 ± 1.9	2.76 ± 0.11	0.27 ± 0.01	109.6 ± 3.4	...
3	C	279 ± 11	$<0.55 \pm 0.02$	$<0.26 \pm 0.01$	117.9 ± 0.4	$>5.2 \pm 0.3$
	D1	49 ± 1	6.26 ± 0.14	124.2 ± 1.4	5.22 ± 0.21	1.62 ± 0.07	134.4 ± 3.6	...

Notes. Columns are as follows: (1) JVN observation epoch; (2) component name; (3) flux density; (4) distance from the origin defined by component C; (5) position angle with respect to the origin (measured from north through east); (6)–(8) parameters of the Gaussian model: FWHM of major and minor axes and the position angle of the major axis; (9) brightness temperature given in the source’s rest frame.

of short-term radio variability is probably associated with the gamma-ray-emitting region.

3.2. JVN Observation Results

Figure 2 shows images of 1H 0323+342 at each epoch. The image parameters are shown in Table 1 along with the total flux density of all CLEAN components. JVN images could not resolve the central one, containing a few components in the images obtained by VLBA, as shown in Section 4. To quantify the relative location and the flux density of each component of the JVN images, we modeled the calibrated images with elliptical Gaussian components. Table 3 shows the model fitting results obtained by the AIPS task JMFIT. The formal errors of

each parameter are estimated using the formula from Fomalont (1999). The data at all epochs are modeled satisfactorily by two distinct components, with the brighter and unresolved component labeled C and the weaker component labeled D1, situated to the southeast of C. The angular size of C, shown in Table 3, is therefore the upper limit. The sum of the flux densities of components C and D1 is in good agreement with both the total CLEANed flux and single-dish measurements by Y32, as shown in Tables 1 and 2, whereas the Very Large Array (VLA) observations at 1.4 GHz on 2006 February 7 and 2007 January 15 (VLA observation code; AP501) show the source having a large-scale structure with a total size of about a hundred kpc (Antón et al. 2008) and with a flux density for the extended

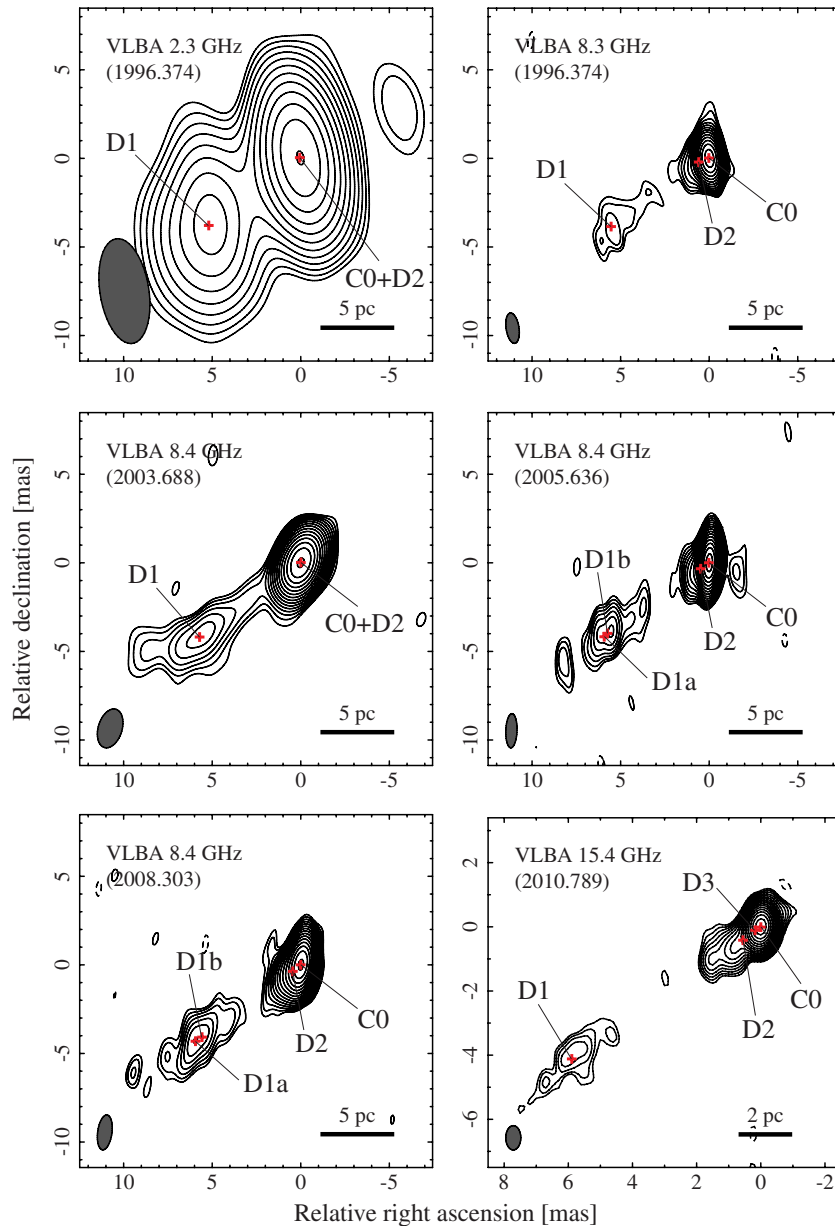


Figure 3. VLBI images of 1H 0323+342 obtained by the VLBA archive data. Top left and bottom right panels show images at 2.3 and 15.4 GHz, respectively, whereas others are at 8 GHz. The lowest contour is three times the off-source rms noise (σ). The dashed and solid curves show negative and positive contours, respectively. The restoring beam is indicated in the lower left corner of each image. The labels C0, D3, D2, and D1 ((a) and (b)) show the Gaussian model fitting components, and the position of each component is indicated by a cross. The image descriptions are given in Table 4.

(A color version of this figure is available in the online journal.)

component of 198 mJy (Doi et al. 2012). We consider that the extended structure has an optically thin spectrum and therefore shows very weak emission at around 8 GHz. It should also be noted that the flux density of component C gradually decreases, similar to the total flux density, whereas the flux density of component D1 seems to be stable, as shown in Figure 1. The results indicate that the short-term radio variability observed with Y32 (and probably the gamma-ray-emitting region) is mainly associated with the central component.

4. VLBA ARCHIVE DATA

To investigate time variation of the pc-scale structure of the source, we reduced the data of the archival VLBA observations at 2, 8, and 15 GHz. The observations are summarized in Table 4. The simultaneous VLBA observation at 2.3 and 8.3 GHz on

1996 May 16 has been published by (Beasley et al. 2002; VLBA observation code; BB023). The 15 GHz observation was carried out as part of the VLBA MOJAVE Program⁸ (Lister et al. 2009) on 2010 October 15, just half a month before the JVN epoch 1 observation. Figure 3 shows images of 1H 0323+342 with VLBA. Descriptions of each image are given in Table 4. The size of the restoring beam for the BK077 observation is slightly larger than those for other observations at 8 GHz since the visibilities with Mauna Kea station, which gives longer-baseline data, are excluded because of inadequate accuracy of the amplitude calibration. All images shown in Figure 3 have a pc-scale structure similar to those of the JVN observations, consisting of two distinct components, with each of them

⁸ See also <http://www.physics.purdue.edu/MOJAVE/>.

Table 4
Observation Summary and Map Description of VLBA Images

Code	Date (Epoch)		ν_{obs} (GHz)	t_{on} (s)	θ_{Bmaj} (mas)	θ_{Bmin} (mas)	P.A. (deg)	S_{peak} (mJy beam $^{-1}$)	σ (mJy beam $^{-1}$)	Contours
(1)	(2)		(3)	(4)	(5)	(6)	(7)	(8)	(9)	(10)
BB023	1996 May 16	(1996.374)	2.269	322	6.00	2.77	9.0	351	2.6	$n = 0, 1, \dots, 11$
	1996 May 16	(1996.374)	8.339	322	1.73	0.73	8.7	245	1.0	$n = 0, 1, \dots, 12$
BK077	2003 Oct 9	(2003.688)	8.421	178	2.26	1.35	-16.9	334	2.5	$n = 0, 1, \dots, 14$
BE042	2005 Aug 20	(2005.636)	8.420	6640	1.93	0.63	-2.0	204	1.3	$n = 0, 1, \dots, 14$
BL156	2008 Apr 20	(2008.303)	8.392	281	1.98	0.81	-7.5	217	1.6	$n = 0, 1, \dots, 14$
BL149	2010 Oct 15	(2010.789)	15.357	2088	0.76	0.47	0.0	223	0.3	$n = 0, 1, \dots, 15$

Notes. Columns are as follows: (1) VLBA observation code; (2) observation date and epoch; (3) observation frequency; (4) total on-source time; (5)–(7) parameters of the restoring beam: FWHM of major and minor axes and the position angle of the major axis; (8) peak intensity; (9) rms noise level; (10) contour levels. The number n corresponds to $-3\sigma, 3\sigma \times (\sqrt{2})^n$.

Table 5
Model Fitting Results for Archival VLBA Observations

Epoch	ν (GHz)	Comp.	S (mJy)	r (mas)	ϕ (deg)	θ_{maj} (mas)	θ_{min} (mas)	P.A. (deg)
(1)	(2)	(3)	(4)	(5)	(6)	(7)	(8)	(9)
1996.374	2.269	C0+D2	389 ± 35	1.33 ± 0.13	1.00 ± 0.10	55.9 ± 0.4
		D1	168 ± 10	6.39 ± 1.31	126.7 ± 1.2	3.80 ± 0.38	2.22 ± 0.22	147.4 ± 1.7
1996.374	8.339	C0	271 ± 11	0.49 ± 0.02	0.14 ± 0.01	125.9 ± 0.2
		D2	51 ± 1	0.58 ± 0.26	110.6 ± 0.4	1.37 ± 0.07	0.13 ± 0.01	131.8 ± 3.0
		D1	40 ± 1	6.70 ± 0.32	125.0 ± 2.4	3.27 ± 0.16	1.43 ± 0.07	138.6 ± 8.2
2003.688	8.421	C0+D2	348 ± 13	0.52 ± 0.02	0.35 ± 0.01	120.5 ± 0.2
		D1	40 ± 1	7.03 ± 0.31	126.3 ± 5.4	3.36 ± 0.13	0.62 ± 0.03	121.0 ± 2.4
2005.636	8.420	C0	203 ± 6	0.35 ± 0.01	0.15 ± 0.01	148.4 ± 0.1
		D2	43 ± 1	0.50 ± 0.21	124.6 ± 0.2	1.48 ± 0.04	0.15 ± 0.01	117.8 ± 1.7
		D1b	13 ± 1	6.93 ± 0.20	124.8 ± 2.0	0.93 ± 0.02	0.30 ± 0.01	107.1 ± 1.5
		D1a	31 ± 1	7.18 ± 0.21	125.4 ± 2.3	5.86 ± 0.33	1.17 ± 0.01	127.3 ± 2.0
2008.303	8.392	C0	179 ± 5	0.30 ± 0.01	0.09 ± 0.01	137.0 ± 0.1
		D2	98 ± 2	0.57 ± 0.21	130.7 ± 0.2	1.35 ± 0.04	0.22 ± 0.01	117.6 ± 0.6
		D1b	29 ± 1	6.86 ± 0.28	126.3 ± 5.1	5.11 ± 0.15	1.09 ± 0.03	127.0 ± 3.1
		D1a	12 ± 1	7.30 ± 0.21	126.0 ± 2.4	1.56 ± 0.05	0.44 ± 0.01	137.3 ± 2.6
2010.789	15.357	C0	193 ± 4	0.18 ± 0.01	0.04 ± 0.01	148.5 ± 0.1
		D3	48 ± 4	0.19 ± 0.19	119.4 ± 0.1	0.20 ± 0.01	0.09 ± 0.01	142.7 ± 0.9
		D2	49 ± 1	0.67 ± 0.24	126.3 ± 0.2	1.97 ± 0.08	0.29 ± 0.01	131.5 ± 2.1
		D1	19 ± 1	7.10 ± 0.27	125.0 ± 2.4	2.77 ± 0.11	0.67 ± 0.03	124.4 ± 11.8

Notes. Columns are as follows: (1) VLBA observation epoch; (2) observation frequency; (3) component name; (4) flux density; (5) distance from the origin defined by component C0; (6) position angle with respect to the origin (measured from north through east); (7)–(9) parameters of the Gaussian model: FWHM of major and minor axes and the position angle of the major axis.

slightly resolved. We modeled the calibrated VLBA images with elliptical Gaussian components. Table 5 shows the model-fitting results. The model-fitting procedure and estimation of errors for each parameter are made in the same manner as those for the JVN data. We could reconstruct VLBA images with three elliptical Gaussian components, C0, D2, and D1, at 8 GHz, and component D1 could be resolved into two components, D1b and D1a, in epochs 2005.636 and 2008.303. In epochs 1996.374 at 2.3 GHz and 2003.688, the images could be modeled by two components because of lower angular resolution than for other epochs. Component C in the JVN images was resolved into two components, C0 and D2, in the VLBA images at 8 GHz. For the 15 GHz image we could find an additional component, D3, in the vicinity of C0.

We also compared the image of JVN epoch 1 with that of the 15 GHz VLBA. We restored the synthesized beam of the VLBA 15 GHz image to the same size as the JVN epoch 1 observation and obtained the flux density of the central component as 276 mJy. The spectral index of $\alpha_8^{15} = -0.70$ is thus derived from the observations by JVN epoch 1 and VLBA MOJAVE.

The radio power at a rest frequency of 8.0 GHz is estimated to be $P_{8\text{GHz}} = 10^{24.6} \text{ W Hz}^{-1}$, where a k correction is applied using α_8^{15} .

5. DISCUSSION

5.1. Brightness Temperature

We have two kinds of radio observations, a single-dish monitoring and VLBI observations; therefore, we can derive brightness temperatures T_{B} from these results using different methods. T_{B} in the source's rest frame can be obtained with an image as

$$T_{\text{B,rest}}^{(\text{image})} = 1.77 \times 10^9 (1+z) \frac{S_{\nu}}{\nu^2 \theta_{\text{maj}} \theta_{\text{min}}} \text{ (K)}, \quad (1)$$

where θ_{maj} (mas) and θ_{min} (mas) are the FWHM sizes of the Gaussian component in the major and minor axes, respectively, and S_{ν} (mJy) is the flux density at an observing frequency ν (GHz). Given the model fitting result of $S_{\nu} = 419 \text{ mJy}$,

$\theta_{\text{maj}} < 1.12$ mas, and $\theta_{\text{min}} < 0.12$ mas for component C at epoch 1, which leads to the highest T_B among our JVN observations, we obtain $T_{B,\text{rest}}^{(\text{image})} > (8.3 \pm 1.3) \times 10^{10}$ K. $T_{B,\text{rest}}^{(\text{image})}$ at the other epochs are shown in Table 3. Linford et al. (2012) made a VLBA observation of the source on 2010 June 30 at 4.8 GHz and estimated the brightness temperature of the core component to be 2.15×10^{10} K, which is comparable to our results.

We can also obtain T_B with the flux variation as

$$T_{B,\text{rest}}^{(\text{var})} = 4.1 \times 10^{10} \left[\frac{D_L}{\Delta t(1+z)} \right]^2 \frac{\Delta S_\nu}{\nu^2} \text{ (K)} \quad (2)$$

(Wagner & Witzel 1995), where D_L (Mpc) is the luminosity distance to the source and ΔS_ν (mJy) is a change in the observed flux density at an observing frequency ν (GHz) during a period of Δt (days). Given the single-dish monitoring result of $\Delta S_\nu = 19$ mJy, $\Delta t = 32$ days and applying $D_L = 270$ Mpc, we obtain $T_{B,\text{rest}}^{(\text{var})} = 7.0 \times 10^{11}$ K. Alternatively, $T_{B,\text{rest}}^{(\text{var})}$ can be estimated by applying the maximum and minimum flux densities during Y32 monitoring, $\Delta S_\nu = 166$ mJy, $\Delta t = 84$ days, and is found to be $T_{B,\text{rest}}^{(\text{var})} = 8.9 \times 10^{11}$ K, which is in good agreement with the above result.

The brightness temperature has been measured for several gamma-ray NLS1s with radio observations. Zhou et al. (2003) analyzed the VLA observation data of a quasar PMN J0948+0022, which is known to have the highest radio loudness in NLS1s, and found the long-term flux variation with a timescale of a few years. The brightness temperature was estimated to be $\sim 10^{13}$ K from the variability. This high T_B was confirmed by Doi et al. (2006b) with their VLBA images and flux variation at 1.7–15.4 GHz, which result in $T_{B,\text{rest}}^{(\text{image})} > 5.5 \times 10^{11} \delta^{-1}$ K and $T_{B,\text{rest}}^{(\text{var})} > 3.3 \times 10^{13} \delta^{-3}$ K, where δ is the Doppler factor. T_B of PMN J0948+0022 was also measured with the global optically connected VLBI (e-VLBI) observation at 22 GHz and was found to be $T_{B,\text{rest}}^{(\text{image})} \sim 3.4 \times 10^{11}$ K (Giroletti et al. 2011). Yuan et al. (2008) compiled previous radio observations for a sample of radio-loud NLS1s and estimated $T_{B,\text{rest}}^{(\text{var})}$ for three gamma-ray sources: 1.1×10^{13} K for SBS 0846+513, 5.1×10^{12} K for PMN J0948+0022, and 3.6×10^{12} K for PKS 1502+036. D’Ammando et al. (2013) found significant flux variation by both single-dish flux monitoring with the Owens Valley Radio Observatory 40 m telescope at 15 GHz and multiepoch VLA observations at eight frequencies from 1.4 to 22.2 GHz, and they estimated $T_{B,\text{rest}}^{(\text{var})}$ to be 2.5×10^{13} K from single-dish measurements. Although our T_B is a few orders of magnitude lower than those mentioned above, it still exceeds the upper limit of T_B assuming the condition of energy equipartition, as shown in Section 5.2, suggesting that acceleration of the radio jet is ongoing in the central engine of the source.

The 8 GHz radio power is estimated to be $P_{8\text{GHz}} = 10^{24.6} \text{ W Hz}^{-1}$, as shown in Section 4, which is much higher than the radio powers at 1.5 GHz of up to $10^{23.7} \text{ W Hz}^{-1}$ measured in a sample of the most radio luminous starburst galaxies (Lonsdale et al. 1993; Smith et al. 1998a, 1998b). This also supports the fact that a nonthermal process in the central region, not a starburst activity, is responsible for the radio emission from 1H 0323+342.

5.2. Doppler Factor

If we assume the condition of energy equipartition between particles and magnetic fields, $T_{B,\text{limit}} \sim 5 \times 10^{10}$ K is derived

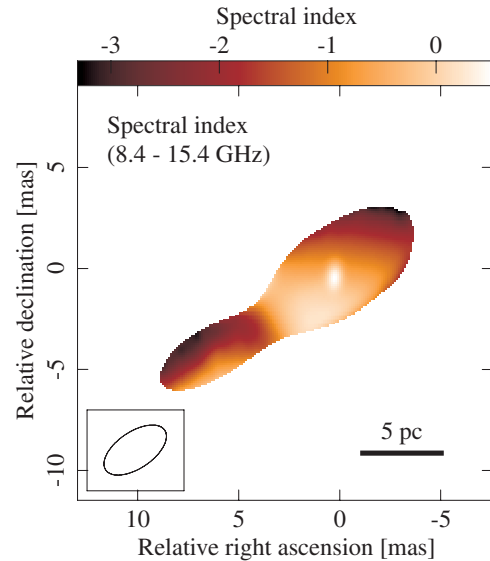


Figure 4. Spectral index map of 1H 0323+342 derived from the flux densities at 8.4 GHz (JVN epoch 1 on 2010 November 1) and 15.4 GHz (VLBA MOJAVE on 2010 October 15). The map corresponds to an area greater than the 3σ noise level in JVN epoch 1. The 15.4 GHz map is restored with the same beam size as the 8.4 GHz map, which is represented in the lower left corner.

(A color version of this figure is available in the online journal.)

as a value for the upper limit in the source’s rest frame (Readhead 1994). The observed $T_{B,\text{rest}}^{(\text{image})}$ for JVN epoch 1 significantly exceeds the limit. Thus, an equipartition Doppler factor, $\delta_{\text{eq}} = T_{B,\text{rest}}^{(\text{image})}/T_{B,\text{limit}}$, of greater than 1.7 should be required to reconcile with our T_B . We can compute the variability Doppler factor as $\delta_{\text{var}} = (1+z)(T_{B,\text{rest}}^{(\text{var})}/T_{B,\text{limit}})^{1/(3-\alpha)}$. Adopting $T_{B,\text{rest}}^{(\text{var})} = 7.0 \times 10^{11}$ K and $\alpha_8^{15} = -0.70$, $\delta_{\text{var}} = 2.2$ can be obtained. Both δ_{eq} and δ_{var} are in good agreement with those obtained by the results with the F-GAMMA Program (Angelakis et al. 2012). These high δ indicate the existence of a highly or mildly relativistic jet(s) in the inner region of the source. This is the third source in which the Doppler beaming effect has been detected in gamma-ray NLS1 by both direct imaging with VLBI and the flux variation, following PMN J0948+0022 (Doi et al. 2006b) and PKS 1502+036 (D’Ammando et al. 2013).

5.3. Spectral Index Distribution

Figure 4 shows the spectral index map of 1H 0323+342 between JVN epoch 1 at 8.4 GHz (2010 November 1) and the VLBA MOJAVE at 15.4 GHz (2010 October 15). Neither observation employs the phase-referencing technique, resulting in the loss of the absolute position through the self-calibration procedure (Pearson & Readhead 1984; Thompson et al. 2001). We therefore superposed two images with reference to the optically thin component D1 since the optically thick central region generally shows the frequency-dependent position shift (e.g., Lobanov 1998a, 1998b). Model fitting to the restored 15.4 GHz MOJAVE image results in a position offset of component D1 at 8.4 and 15.4 GHz with respect to component C of $\Delta\alpha = 0.2$ mas and $\Delta\delta = 0.3$ mas in right ascension and declination, respectively. The compact central region with a size of 0.6 mas, or 0.7 pc, shows an optically thick spectral feature as it becomes steeper along the stream of the jet. Figure 5 shows the spectral index distribution given by a position angle of $122^\circ 8'$, corresponding to the direction of component D1 with respect to C at JVN epoch 1. Error bars for each point in Figure 5

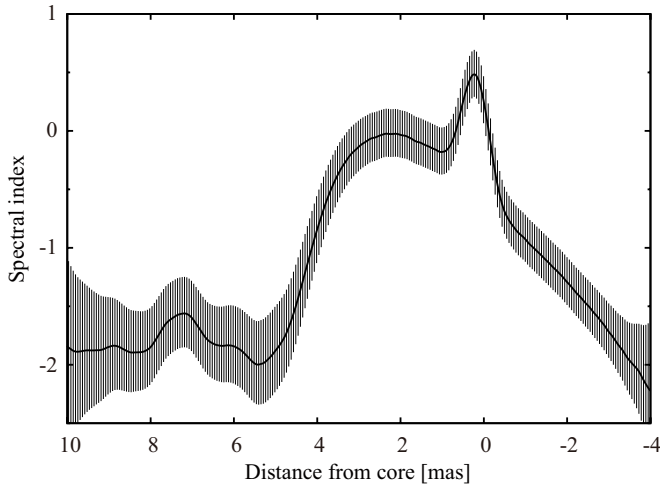


Figure 5. Spectral index distribution given by the position angle of $122^\circ 8$. The horizontal axis shows the angular separation from the center position of component C. A positive value corresponds to the southeastern direction.

are estimated by the image rms and the amplitude calibration error of each image. The maximum of the spectral index at the innermost region is $\alpha = 0.42 \pm 0.20$, showing the central region has an inverted or flat spectrum at even higher frequencies. This feature is similar to that of blazars, suggesting that the source has activities due to relativistic jets.

5.4. Proper Motion of Each Component

Figure 6 shows the distance of components D2 and D1 (a, b) from the core (C or C0) as a function of the observed epoch. Although we cannot identify component D1 with either D1a or D1b, if we adopt the identification of D1 with D1a, an apparent proper motion of $-0.115 \pm 0.083 \text{ mas yr}^{-1}$ is obtained by a weighted least-squares linear fit to component D1, corresponding to an apparent velocity v_{app} of $(-0.45 \pm 0.32)c$. If we exclude the points for JVN epochs 2 and 3 for a linear fit to D1, an apparent proper motion of $0.031 \pm 0.011 \text{ mas yr}^{-1}$ is obtained, corresponding to $v_{\text{app}} = (0.12 \pm 0.04)c$. For component D2, the apparent proper motion is $0.004 \pm 0.008 \text{ mas yr}^{-1}$, corresponding to $v_{\text{app}} = (0.02 \pm 0.03)c$. If we omit the data point at 1996.374, the apparent proper motion becomes $0.033 \pm 0.004 \text{ mas yr}^{-1}$, corresponding to $v_{\text{app}} = (0.13 \pm 0.02)c$, which is similar to that for component D1. We cannot determine whether component D1 at epoch 1996.374 and at other epochs is identical since no VLBI observation was performed from 1996.374 to 2003.688. Future multiepoch and intensive VLBI observations will make an identification and a measurement of precise proper motion of D1. In either case, our results show that both components D2 and D1 are stationary or have very low speeds compared to typical (gamma-ray) blazars (e.g., Jorstad et al. 2001).

5.5. Relation to General Properties of NLS1s

As shown in Section 1, NLS1s are generally considered to have higher accretion rates and lower jet activities compared to other types of radio-loud AGNs (Greene et al. 2006; Zhou et al. 2006). In the analogy of X-ray binaries with $M_{\text{BH}} \sim 10 M_{\odot}$, radio emission is quenched when the luminosity is from a few percent to about 10% of the Eddington rate, corresponding to the high/soft state, whereas the jet emerges when the luminosity is nearly equal to the Eddington rate, corresponding to a very high

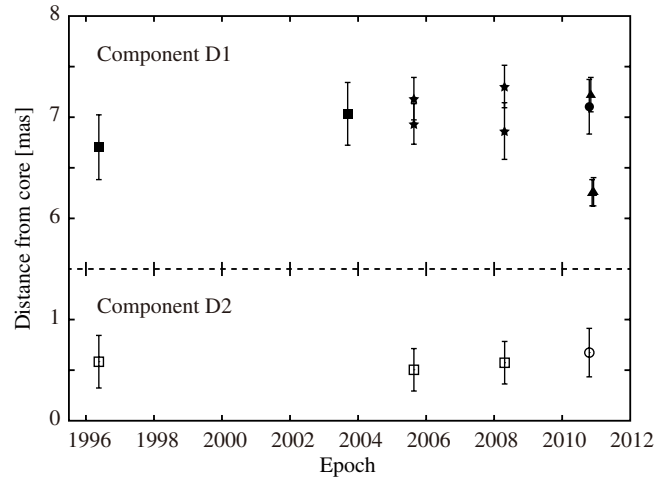


Figure 6. Distance of components D2 and D1 ((a) and (b)) from component C (for JVN observations) or C0 (for VLBA observations) as a function of the observed epoch. See Tables 3 and 5 for numerical values. The open and filled symbols are for components D2 and D1, respectively. The squares and circles represent the VLBA results at 8 and 15 GHz, respectively, and stars correspond to components D1a and D1b at epochs 2005.636 and 2008.303. The triangles represent the JVN results.

state (Maccarone et al. 2003; Fender et al. 2004). 1H 0323+342 has both highly or mildly relativistic jets in the innermost region, as revealed by our observations, and an extremely high accretion rate with an accretion disk luminosity of $0.9 L_{\text{Edd}}$ (Abdo et al. 2009b). These characteristics imply that the state transition of the source is in accordance with that of Galactic X-ray binaries.

On the other hand, 1H 0323+342 has a very high accretion rate with a smaller black hole mass of $\sim 10^7 M_{\odot}$ (Zhou et al. 2007; Abdo et al. 2009b), and it also shows a very radio-loud feature of $R_{1.4} = 318$ (Foschini 2011), or $R_5 = 246$ (Doi et al. 2012). These properties seem to be contrary to previous studies showing a correlation between radio loudness and the black hole mass (McLure & Jarvis 2004 and references therein) and an anticorrelation between radio loudness and the accretion rate (Greene et al. 2006 and references therein) for a large sample of AGNs. Following these correlations, 1H 0323+342 may intrinsically be a radio-quiet one but seems to be radio loud as a result of the Doppler boosting effect, as similar results have been obtained for several radio-loud NLS1s (Doi et al. 2011, 2012). The observed radio flux density is boosted by a factor of $D = \delta^{3-\alpha}$, and we obtain $D = 18.5$ when applying $\delta = 2.2$ and $\alpha = -0.70$ derived from our studies. Thus, the intrinsic radio loudness can be estimated as $R_{1.4}^{(\text{int})} = 17$ and $R_5^{(\text{int})} = 13$. Although these R are still in the radio-loud regime ($R > 10$; Kellermann et al. 1989), 1H 0323+342 intrinsically has a much lower R than expected.

5.6. Radio Spectrum

Figure 7 shows the composite radio spectrum of 1H 0323+342, including not only our VLBI observation results but also previous single-dish or interferometric measurements. We applied spectral fitting to the VLBI data with a synchrotron self-absorption (SSA) spectral model, $S_{\nu} = S_0 \nu^{2.5} [1 - \exp(-\tau_{\text{ss}} \nu^{\alpha-2.5})]$, where S_0 is a scaling constant and τ_{ss} is the SSA coefficient. In the SSA fit to the sum of the flux of all VLBI components, a peak flux density S_m of 0.72 Jy is derived at a turnover frequency ν_m of 3.5 GHz, as shown in Figure 7(a), while the source is separated into two or more components in Figures 2 and 3. If we apply the SSA fit to each VLBI

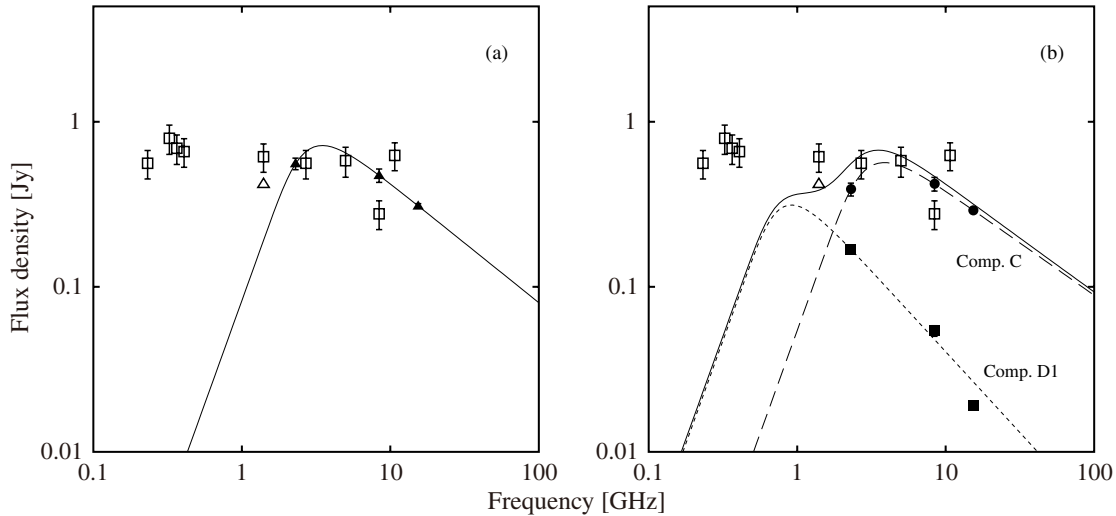


Figure 7. Composite radio spectrum of 1H 0323+342. The filled symbols represent the VLBI results at 2.3 GHz (VLBA), 8.4 GHz (JVN epoch 1), and 15.4 GHz (VLBA), whereas the open squares are the total flux density by single-dish or radio interferometer. The open triangle indicates the flux density of the core component obtained by VLA (Doi et al. 2012). (a) Radio spectrum for the sum of flux for all VLBI components. The solid line represents the best-fit curve with the synchrotron spectrum. (b) Radio spectra for components C and D1. The filled circles and squares are VLBI results for components C (or C0 + D3 + D2 for VLBA) and D1, respectively. The dashed and dotted lines represent the best-fit curve with the synchrotron spectrum for components C and D1, respectively, and the solid line describes the sum of two synchrotron spectra. A turnover frequency of 0.9 GHz is assumed for the spectral fitting to component D1 (see also Section 5.7). Single-dish and interferometer measurement data are from Colla et al. (1973), Condon et al. (1998), Douglas et al. (1996), Healey et al. (2007), Neumann et al. (1994), Reich et al. (2000), Rengelink et al. (1997), and Zhang et al. (1997). Part of the flux data is compiled from the SPECIND V2.0 catalog (Vollmer et al. 2010).

component, as shown in Figure 7(b), $S_m = 0.57$ Jy is derived at $\nu_m = 3.9$ GHz for component C. Here ν_m can be given under the condition of a homogeneous, self-absorbed, and incoherent synchrotron radio source with a power-law electron energy distribution of

$$\nu_m \sim 8B^{1/5}S_m^{2/5}\theta^{-4/5}(1+z)^{1/5} \text{ (GHz)} \quad (3)$$

(Kellermann & Pauliny-Toth 1981), where B (G) is the magnetic field and θ (mas) is the angular size of a source. Applying $\nu_m = 3.9$ GHz and $S_m = 0.57$ Jy given by the SSA fitting results and $\theta = \sqrt{\theta_{\text{maj}}\theta_{\text{min}}} \sim 0.4$ mas from VLBI observations, we can derive $B \sim 2$ mG, which is comparable to the magnetic field for young radio galaxies (e.g., Murgia et al. 1999). For component D1, $S_m = 0.31$ Jy is derived assuming $\nu_m = 0.9$ GHz in the spectral fitting in Figure 7(b). Applying $B \sim 2$ mG derived for component C and $\theta \sim 2$ mas, we obtain $S_m \sim 0.37$ Jy from Equation (3), which is comparable to that given by the SSA fitting. Although Equation (3) depends strongly on the parameters, component D1 shows similar ν_m or S_m between the spectral fitting and numerical estimation. In Figure 7(b), the sum of two synchrotron spectra accounts for the total flux measurements at a frequency of greater than 1 GHz. Particularly, the total flux of the central component detected by VLA at 1.4 GHz (open triangle in Figure 7; Doi et al. 2012) accounts for the sum of the flux of two VLBI components, implying that the emission of the VLA central component mainly comes from the pc-scale VLBI components. However, the composite spectrum for the VLBI components cannot account for the points in the MHz frequency range. These emissions probably come from extended, optically thin components on the kpc-scale detected with interferometric observations, as discussed in Section 5.7.

We should point out that the composite radio spectrum shown in Figure 7 is not obtained simultaneously. Future multifrequency, simultaneous, and high-resolution VLBI observations are thus important to reveal the spectral properties of the innermost region precisely.

5.7. Possibility of a Young Radio Source and Recurrent Jet Activity

Some previous studies point out similarities between NLS1s and young radio galaxies, such as gigahertz-peaked spectrum sources (GPSs; O’Dea 1998), in terms of compact and stable radio morphologies and a steep spectrum of an inner region (e.g., Gallo et al. 2006; Komossa et al. 2006). As shown in Section 5.4, the JVN observations combined with the archival VLBA data revealed the existence of two stationary or slowly moving components, D2 and D1, and Zhou et al. (2007) mention that component D1 is possibly a weak radio lobe.

The viewing angle of the component ϕ can be obtained using the apparent velocity $\beta_{\text{app}} \equiv v_{\text{app}}/c$ and a Doppler factor δ as

$$\phi = \tan^{-1} \frac{2\beta_{\text{app}}}{\beta_{\text{app}}^2 + \delta^2 - 1} \quad (4)$$

(Ghisellini et al. 1993). If component D1 has the same δ as C and we adopt $\delta = 2.2$, as derived in Section 5.2, we can obtain $\phi = 3^\circ.6$, which is in good agreement with $\phi = 3^\circ$ derived by the model fitting to the spectral energy distribution (Abdo et al. 2009b). We can also calculate the real distance between C and D1 as 0.13 kpc. Assuming linear expansion of components D2 and D1 with a constant apparent velocity of $0.02c$ and $0.12c$, respectively, as shown in Section 5.4, a kinematic age t_{kin} of 120 and 220 yr is derived for the respective components. A similar source age can be estimated from a correlation between the linear size and ν_m of a source (O’Dea & Baum 1997). Thus, we believe that the pc-scale structure in 1H 0323+342 detected by VLBI observations has GPS-like features in terms of the GHz-peaked spectrum, as shown in Figure 7, the young age of $\sim 10^2$ yr, and the compact structure of ~ 0.1 kpc.

On the other hand, previous VLA observations show $t_{\text{kin}} \sim 10^7$ – 10^8 yr for the 100 kpc scale structure detected by the VLA C-array configuration (Antón et al. 2008; Doi et al. 2012), whereas $t_{\text{kin}} \sim 10^6$ – 10^7 yr can be estimated for the extended structure with a scale of 20 kpc detected by the VLA A-array

configuration. The VLA images also show the extended structure with a position angle of $\sim 45^\circ$ with the 100 kpc scale and $\sim 90^\circ$ with the 20 kpc scale (Antón et al. 2008), both of which are significantly different from that of $\sim 125^\circ$ with pc-scale images obtained by VLBI observations. Additionally, no extended feature could be found by the JVN observations within the field of view of a few hundred mas (corresponding to a kinematic age of $\sim 10^4$ yr) under the condition of a detection limit three times the rms image noise. The difference in the estimated kinetic age for components D2, D1, and the Kiloparsec-scale structures, as well as the fact that no extended feature could be found by the JVN observations within a field of view of a few hundred mas, imply that the pc-scale jet structure represents recurrent jet activity (e.g., Baum et al. 1990; Augusto et al. 2006; Doi et al. 2013b). In fact, the 8 GHz radio power for the pc-scale components is $P_{8\text{GHz}} = 10^{24.6} \text{ W Hz}^{-1}$, as shown in Section 4, and the jet kinetic power is roughly estimated to be $\sim 10^{44} \text{ erg s}^{-1}$ from $P_{8\text{GHz}}$, which is enough to make the source grow to the size of a hundred kpc (Doi et al. 2012, 2013a). The extremely large difference in the position angle between the kpc and pc scales may be the projection effect of extended components due to the small viewing angle.

5.8. Possibility of Free–Free Absorption

Free–free absorption could be an explanation for an apparent asymmetric structure, and previous VLBI observations have revealed the existence of free–free absorption in several GPSs (e.g., Kamen et al. 2000, 2001; Marr et al. 2001). The optical depth of free–free absorption can be estimated as

$$\tau_{\text{ff}} = 8.235 \times 10^{-2} T_e^{-1.35} \nu^{-2.1} \int_{\text{LOS}} n_e^2 dl \quad (5)$$

(Mezger & Henderson 1967), where T_e (K) and n_e (cm^{-3}) are the electron temperature and density of the absorber, ν (GHz) is the frequency, and l (pc) is the path length via the line of sight. The peak intensity of component D1 is 38 mJy beam^{-1} on the image of JVN epoch 1, resulting in an attenuation of more than a factor of 4.1 if we assume an intrinsic jet symmetry and a detection limit of the counter component of three times the rms image noise. A τ_{ff} greater than 1.4 is thus required to reconcile with the observed asymmetry. Assuming $T_e > 8000 \text{ K}$ for the fully ionized condition, $l = 0.13 \text{ kpc}$ for the distance between components C and D1, and $\nu = (1+z) \times 8.4 = 8.9 \text{ GHz}$, a column density of electrons $N_e = n_e l > 6 \times 10^{23} \text{ cm}^{-2}$ is required. This N_e is two orders of magnitude larger than the Galactic H I column density of $1.349 \times 10^{21} \text{ cm}^{-2}$ obtained by the ROSAT All-Sky Survey (Voges et al. 1999). Moreover, the kpc-scale radio morphology of the source seems to be an asymmetric structure elongated to the east, as shown by Antón et al. (2008), although they consider the morphology to be a core plus a two-sided structure. As shown in Section 5.5, we obtain $D = 18.5$ as a boosting factor for the radio flux. This D is accountable for the observed flux ratio of approaching to receding jet components mentioned above. We therefore conclude that the asymmetric structure detected by the JVN observations is not due to free-free absorption but due to the Doppler beaming effect.

5.9. Gamma-Ray Emission from 1H 0323+342

Marscher et al. (2008) analyzed the multiwavelength light curve and quasi-simultaneous multiepoch VLBI images of a blazar BL Lacertae and proposed the inner jet model to explain

the flare timing between each energy band and the sudden change in the optical polarization position angle. They suggest that the flare is stimulated by the passage of the emission feature through the conical standing shock at around $10^5 R_s$ from the central black hole, where R_s is the Schwarzschild radius, and the gamma-ray flare would occur in this area. $10^5 R_s$ corresponds to a linear scale of 0.1 pc or an angular size of 0.08 mas for 1H 0323+342. Although our observations combined with the archival VLBA results reveal the existence of the relativistic jet in the innermost region and stationary or slowly moving components D2 and D1, as shown in Section 5.4, the linear distance of D2 and D1 from C0 is $10^7 R_s$ and $10^8 R_s$, respectively, assuming ϕ from our results. The central black hole may be located upstream of the core at 8 GHz as a result of the frequency-dependent position shift; thus, the distance between the central black hole and components D2 and D1 is farther than those mentioned above. On the other hand, the linear scale of $10^5 R_s$ is comparable to the light-crossing distance corresponding to the timescale of the short-term radio variability ($0.3 \times 10^5 R_s$), which is probably associated with component C (and the gamma-ray-emitting region), as shown in Section 3.2. Moreover, the VLBA image at 15 GHz shown in Figure 3 indicates the existence of a component D3 in the vicinity of component C0, with a separation angle of 0.19 mas, or a linear distance of $2 \times 10^5 R_s$. Proper motion and flux variation of component D3 might be related to the gamma-ray flux, and future high-resolution and high-sensitivity VLBI observations will be important to investigate the gamma-ray emission mechanism from NLS1s.

Gamma-ray emission has been detected from blazars with a larger Doppler factor and a smaller viewing angle (e.g., $\delta \gtrsim 14$ and $\phi < 4^\circ$ for PKS 1741–038; Wajima et al. 2000) and with a smaller Doppler factor and a larger viewing angle (e.g., $\delta \sim 2.5$ and $\phi = 23^\circ$ for PKS 1622–297; Wajima et al. 2006). Both blazars have superluminal jet components and thus show very high intrinsic velocities with $\beta > 0.9$, implying that the inverse-Compton process plays a key role for gamma-ray emission. On the other hand, 1H 0323+342 has smaller δ , β , and ϕ and thus seems to have different features compared to typical gamma-ray blazars. Future simultaneous, multiwavelength observations from radio to gamma-ray and high-resolution polarization studies will be key issues to reveal the gamma-ray emission mechanism from NLS1s.

6. CONCLUSION

We made simultaneous single-dish and VLBI observations of gamma-ray NLS1 galaxy 1H 0323+342 at 8 GHz. The achievements of our study can be summarized as follows.

1. We found significant flux variation on the timescale of one month with single-dish monitoring by the Yamaguchi 32 m radio telescope. The total flux density varied by 5.5% over 32 days, corresponding to a variability brightness temperature of $7.0 \times 10^{11} \text{ K}$.
2. Milliarcsecond-scale images obtained by three-epoch Japanese VLBI Network observations show that the source has a compact core-jet structure similar to that of blazars. The visibilities can be modeled satisfactorily by two elliptical Gaussian components. Only the central component shows a flux decrease similar to that of the total flux obtained with the single-dish monitoring, whereas the flux density of the southeastern component seems to be stable.

3. Two year *Fermi*/LAT monitoring results show that the source has gamma-ray flux variation on a timescale similar to our single-dish monitoring results. By combining results 1 and 2, we conclude that the source of short-term radio variability is probably associated with the gamma-ray-emitting region.
4. The brightness temperature obtained by the JVN observations is greater than $(5.2 \pm 0.3) \times 10^{10}$ K, and the radio power at 8 GHz is estimated to be $10^{24.6}$ W Hz⁻¹. These values indicate that a nonthermal process in the central region is responsible for the radio emission from the source.
5. The Doppler factor is estimated to be $\delta_{\text{eq}} > 1.7$ assuming the condition of energy equipartition in the JVN observations, and $\delta_{\text{var}} = 2.2$ from the observed radio variability, indicating the existence of a relativistic jet(s). This is the third source in which the Doppler beaming effect is detected in gamma-ray NLS1s by both direct imaging with VLBI and the flux variation.
6. The JVN observations revealed the existence of Doppler boosted jet components that affect the radio loudness of the source. Although the source shows extremely high apparent radio loudness with $R > 200$, the intrinsic R is less than 20 when applying the Doppler factor obtained by the JVN observations. Hence, for 1H 0323+342 with a smaller black hole mass ($\sim 10^7 M_{\odot}$) and high accretion rate ($\sim 0.9 L_{\text{Edd}}$), there seems to be no large discrepancy with previous studies, suggesting a correlation between R and the black hole mass and an anticorrelation between R and the accretion rate.
7. Multiepoch JVN and VLBA images detected slowly moving jet components D2 and D1 with apparent velocities of $(0.02 \pm 0.03)c$ and $(0.12 \pm 0.04)c$, respectively, and the real distance between components C and D1 was estimated as 0.13 kpc. A kinematic age of $\sim 10^2$ yr is derived for both components assuming the linear expansion, which is significantly different from that of kpc-scale components ($\sim 10^7$ – 10^8 yr). By combining the results of the spectral fitting to the flux measurements and observed properties in terms of the position angle and the lack of medium-scale radio emission, we conclude that the pc-scale jet structure represents recurrent jet activity.

We are grateful to the anonymous referee for valuable comments, which improved the manuscript. The JVN project is led by the National Astronomical Observatory of Japan (NAOJ), which is a branch of the National Institutes of Natural Sciences (NINS), Hokkaido University, Ibaraki University, University of Tsukuba, Gifu University, Osaka Prefecture University, Yamaguchi University, and Kagoshima University, in cooperation with the Geospatial Information Authority of Japan (GSI), the Japan Aerospace Exploration Agency (JAXA), and the National Institute of Information and Communications Technology (NICT). The VLBA is operated by the National Radio Astronomy Observatory, which is a facility of the National Science Foundation operated under cooperative agreement by Associated Universities, Inc. This research has made use of the following data, tools, and facilities: the data from the MOJAVE database that is maintained by the MOJAVE team (Lister et al. 2009), the Swinburne University of Technology software correlator (Deller et al. 2011), NASA's Astrophysics Data System Abstract Service, the NASA/IPAC Extragalactic Database (NED), which is operated by the Jet Propulsion Laboratory, Ned Wright's online cosmology calculator, and the Vizier catalog

access tool, CDS, Strasbourg, France (Ochsenbein et al. 2000). This work is partly supported by the National Natural Science Foundation of China (grant 11121062), the CAS/SAFEA International Partnership Program for Creative Research Teams, and the Strategic Priority Research Program on Space Science, Chinese Academy of Sciences (grant XDA04060700).

REFERENCES

- Abdo, A. A., Ackermann, M., Ajello, M., et al. 2009a, *ApJ*, **699**, 976
- Abdo, A. A., Ackermann, M., Ajello, M., et al. 2009b, *ApJL*, **707**, L142
- Angelakis, E., Fuhrmann, L., Nestoras, I., et al. 2012, arXiv:1205.1961
- Antón, S., Browne, I. W. A., & Marchã, M. J. 2008, *A&A*, **490**, 583
- Augusto, P., Gonzalez-Serrano, J. I., Perez-Fournon, I., & Wilkinson, P. N. 2006, *MNRAS*, **368**, 1411
- Baum, S. A., O'Dea, C. P., Murphy, D. W., & de Bruyn, A. G. 1990, *A&A*, **232**, 19
- Beasley, A. J., Gordon, D., Peck, A. B., et al. 2002, *ApJS*, **141**, 13
- Borison, T. A. 2002, *ApJ*, **565**, 78
- Calderone, G., Foschini, L., Ghisellini, G., et al. 2011, *MNRAS*, **413**, 2365
- Colla, G., Fanti, C., Fanti, R., et al. 1973, *A&AS*, **11**, 291
- Condon, J. J., Cotton, W. D., Greisen, E. W., et al. 1998, *AJ*, **115**, 1693
- D'Ammando, F., Orienti, M., Doi, A., et al. 2013, *MNRAS*, **433**, 952
- D'Ammando, F., Orienti, M., Finke, J., et al. 2012, *MNRAS*, **426**, 317
- Deller, A. T., Briske, W. F., Phillips, C. J., et al. 2011, *PASP*, **123**, 275
- Doi, A., Asada, K., Fujisawa, K., et al. 2013a, *ApJ*, **765**, 69
- Doi, A., Asada, K., & Nagai, H. 2011, *ApJ*, **738**, 126
- Doi, A., Fujisawa, K., Harada, K., et al. 2006a, in Proc. 8th European VLBI Network Symp., ed. W. Baan, R. Bachiller, R. Booth et al. (Bonn: MPIfR), **71**
- Doi, A., Fujisawa, K., Inoue, M., et al. 2007, *PASJ*, **59**, 703
- Doi, A., Murata, Y., Mochizuki, N., et al. 2013b, *PASJ*, **65**, 57
- Doi, A., Nagai, H., Asada, K., et al. 2006b, *PASJ*, **58**, 829
- Doi, A., Nagira, H., Kawakatu, N., et al. 2012, *ApJ*, **760**, 41
- Douglas, J. N., Bash, F. N., Bozayan, F. A., Torrence, G. W., & Wolfe, C. 1996, *AJ*, **111**, 1945
- Fender, R. P., Belloni, T. M., & Gallo, E. 2004, *MNRAS*, **355**, 1105
- Fomalont, E. B. 1999, in ASP Conf. Ser. 180, Synthesis Imaging in Radio Astronomy II, ed. G. B. Taylor, C. L. Carilli, & R. A. Perley (San Francisco, CA: ASP), **301**
- Foschini, L. 2011, in Narrow-Line Seyfert 1 Galaxies and Their Place in the Universe, ed. L. Foschini, M. Colpi, L. Gallo et al. (Trieste: PoS), **024**
- Fuhrmann, L., Angelakis, E., Nestoras, I., et al. 2011, in Narrow-Line Seyfert 1 Galaxies and Their Place in the Universe, ed. L. Foschini, M. Colpi, L. Gallo et al. (Trieste: PoS), **026**
- Fujisawa, K., Mashiyama, H., Shimoikura, T., & Kawaguchi, N. 2002, in Proc. IAU 8th Asian-Pacific Regional Meeting, Vol. 2, ed. S. Ikeuchi, J. Hearnshaw, & T. Hanawa (Tokyo: Astron. Soc. Japan), **3**
- Gallo, L. C., Edwards, P. G., Ferrero, E., et al. 2006, *MNRAS*, **370**, 245
- Ghisellini, G., Padovani, P., Celotti, A., & Maraschi, L. 1993, *ApJ*, **407**, 65
- Giroletti, M., Paragi, Z., Bignall, H., et al. 2011, *A&A*, **528**, L11
- Greene, J. E., Ho, L. C., & Ulvestad, J. S. 2006, *ApJ*, **636**, 56
- Greisen, E. W. 2003, in Information Handling in Astronomy—Historical Vistas, ed. A. Heck (Dordrecht: Kluwer), **109**
- Hartman, R. C., Bertsch, D. L., Bloom, S. D., et al. 1999, *ApJS*, **123**, 79
- Healey, S. E., Romani, R. W., Taylor, G. B., et al. 2007, *ApJS*, **171**, 61
- Jorstad, S. G., Marscher, A. P., Mattox, J. R., et al. 2001, *ApJS*, **134**, 181
- Kadota, A., Fujisawa, K., Sawada-Satoh, S., Wajima, K., & Doi, A. 2012, *PASJ*, **64**, 109
- Kamen, S., Horiuchi, S., Shen, Z.-Q., et al. 2000, *PASJ*, **52**, 209
- Kamen, S., Sawada-Satoh, S., Inoue, M., Shen, Z.-Q., & Wajima, K. 2001, *PASJ*, **53**, 169
- Kellermann, K. I., & Pauliny-Toth, I. I. K. 1981, *ARA&A*, **19**, 373
- Kellermann, K. I., Sramek, R., Schmidt, M., Shaffer, D. B., & Green, R. 1989, *AJ*, **98**, 1195
- Kobayashi, H., Sasao, T., Kawaguchi, N., et al. 2003, in ASP Conf. Ser. 306, New Technologies in VLBI, ed. Y. C. Minh (San Francisco, CA: ASP), **48**
- Komatsu, E., Dunkley, J., Nolte, M. R., et al. 2009, *ApJS*, **180**, 330
- Komossa, S., Voges, W., Xu, D., et al. 2006, *AJ*, **132**, 531
- Linford, J. D., Taylor, G. B., Romani, R. W., et al. 2012, *ApJ*, **744**, 177
- Lister, M. L., Aller, H. D., Aller, M. F., et al. 2009, *AJ*, **137**, 3718
- Lobanov, A. P. 1998a, *A&A*, **330**, 79
- Lobanov, A. P. 1998b, *A&AS*, **132**, 261
- Lonsdale, C. J., Smith, H. E., & Lonsdale, C. J. 1993, *ApJL*, **405**, L9
- Maccarone, T. J., Gallo, E., & Fender, R. 2003, *MNRAS*, **345**, L19

- Marchã, M. J. M., Browne, I. W. A., Impey, C. D., & Smith, P. S. 1996, *MNRAS*, **281**, 425
- Marr, J. M., Taylor, G. B., & Crawford, F., III 2001, *ApJ*, **550**, 160
- Marscher, A. P., Jorstad, S. G., D’Arcangelo, F. D., et al. 2008, *Natur*, **452**, 966
- McLure, R. J., & Jarvis, M. J. 2004, *MNRAS*, **353**, L45
- Mezger, P. G., & Henderson, A. P. 1967, *ApJ*, **147**, 471
- Mineshige, S., Kawaguchi, T., Takeuchi, M., & Hayashida, K. 2000, *PASJ*, **52**, 499
- Murgia, M., Fanti, C., Fanti, R., et al. 1999, *A&A*, **345**, 769
- Neumann, M., Reich, W., Fürst, E., et al. 1994, *A&AS*, **106**, 303
- Nolan, P. L., Abdo, A. A., Ackermann, M., et al. 2012, *ApJS*, **199**, 31
- Ochsenbein, F., Bauer, P., & Marcout, J. 2000, *A&AS*, **143**, 23
- O’Dea, C. P. 1998, *PASP*, **110**, 493
- O’Dea, C. P., & Baum, S. A. 1997, *AJ*, **113**, 148
- Orienti, M., D’Ammando, F., & Giroletti, M. (for the *Fermi*-LAT Collaboration). 2012, arXiv:1205.0402
- Osterbrock, D. E., & Pogge, R. W. 1985, *ApJ*, **297**, 166
- Ott, M., Witzel, A., Quirrenbach, A., et al. 1994, *A&A*, **284**, 331
- Pearson, T. J., & Readhead, A. C. S. 1984, *ARA&A*, **22**, 97
- Pogge, R. W. 2000, *NewAR*, **44**, 381
- Readhead, A. C. S. 1994, *ApJ*, **426**, 51
- Reich, W., Fürst, E., Reich, P., et al. 2000, *A&A*, **363**, 141
- Rengelink, R. B., Tang, Y., de Bruyn, A. G., et al. 1997, *A&AS*, **124**, 259
- Shepherd, M. C. 1997, in ASP Conf. Ser. 125, *Astronomical Data Analysis Software and Systems VI*, ed. G. Hunt & H. E. Payne (San Francisco, CA: ASP), 77
- Shibata, K. M., Kameno, S., Inoue, M., & Kobayashi, H. 1998, in ASP Conf. Ser. 144, *IAU Colloq. 164: Radio Emission from Galactic and Extragalactic Compact Sources*, ed. J. A. Zensus, G. B. Taylor, & J. M. Wrobel (San Francisco, CA: ASP), 413
- Smith, D. A., Herter, T., & Haynes, M. P. 1998a, *ApJ*, **494**, 150
- Smith, H. E., Lonsdale, C. J., & Lonsdale, C. J. 1998b, *ApJ*, **492**, 137
- Sowards-Emmerd, D., Romani, R. W., & Michelson, P. F. 2003, *ApJ*, **590**, 109
- Sowards-Emmerd, D., Romani, R. W., Michelson, P. F., & Ulvestad, J. S. 2004, *ApJ*, **609**, 564
- Thompson, A. R., Moran, J. M., & Swenson, G. W., Jr. 2001, *Interferometry and Synthesis in Radio Astronomy*, (2nd ed.; New York: John Wiley & Sons)
- Voges, W., Aschenbach, B., Boller, Th., et al. 1999, *A&A*, **349**, 389
- Vollmer, B., Gassmann, B., Derrière, S., et al. 2010, *A&A*, **511**, 53
- Wagner, S. J., & Witzel, A. 1995, *ARA&A*, **33**, 163
- Wajima, K., Bignall, H. E., Kobayashi, H., et al. 2006, *PASJ*, **58**, 223
- Wajima, K., Lovell, J. E. J., Kobayashi, H., et al. 2000, *PASJ*, **52**, 329
- Yonekura, Y., Saito, Y., Saito, T., et al. 2013, in ASP Conf. Ser. 476, *New Trends in Radio Astronomy in the ALMA Era*, ed. R. Kawabe & N. Kuno (San Francisco, CA: ASP), 415
- Yuan, W., Zhou, H. Y., Komossa, S., et al. 2008, *ApJ*, **685**, 801
- Zhang, X., Zheng, Y., Chen, H., et al. 1997, *A&AS*, **121**, 59
- Zhou, H.-Y., Wang, T.-G., Dong, X.-B., Zhou, Y.-Y., & Li, C. 2003, *ApJ*, **584**, 147
- Zhou, H.-Y., Wang, T.-G., Yuan, W.-M., et al. 2006, *ApJS*, **166**, 128
- Zhou, H.-Y., Wang, T.-G., Yuan, W.-M., et al. 2007, *ApJL*, **658**, L13